Mechanism of glycogen synthase inactivation and interaction with glycogenin

Laura Marr [a], Dipsikha Biswas [b], Leonard A. Daly [c], Christopher Browning [d], Sarah Vial [d], Daniel P. Maskell [a], Catherine Hudson [d], John Pollard [d], Jay Bertrand [d], Neil A. Ranson [a], Heena Khatter [d], Claire E. Eyers [c], Kei Sakamoto [b], Elton Zeqiraj [a]*

[a] Astbury Centre for Structural Molecular Biology, School of Molecular and Cellular Biology, Faculty of Biological Sciences, University of Leeds, Leeds, UK

[b] Novo Nordisk Foundation Center for Basic Metabolic Research, University of Copenhagen, Copenhagen, Denmark

[c] Department of Biochemistry and Systems Biology, Institute of Systems, Molecular and Integrative Biology, University of Liverpool, Liverpool, UK

[d] Vertex Pharmaceuticals Inc., Milton Park, Abingdon, UK

*Correspondence to: e.zeqiraj@leeds.ac.uk

Abstract (150 words max)

Glycogen is the major glucose reserve in eukaryotes, and defects in glycogen metabolism and structure lead to disease. Glycogenesis involves interaction of glycogenin (GN) with glycogen synthase (GS), where GS is activated by glucose-6-phosphate (G6P) and inactivated by phosphorylation. We describe the 2.6 Å resolution cryo-EM structure of phosphorylated human GS revealing an autoinhibited GS tetramer flanked by two GN dimers. Phosphorylated N- and C-termini from two GS protomers converge near the G6P-binding pocket and buttress against GS regulatory helices. This keeps GS in an inactive conformation mediated by phospho-Ser641 interactions with a composite “arginine cradle”. Structure-guided mutagenesis perturbing interactions with phosphorylated tails led to increased basal/unstimulated GS activity. We propose that multivalent phosphorylation supports GS autoinhibition through interactions from a dynamic “spike” region, allowing a tuneable rheostat for regulating GS activity. This work therefore provides new insights into glycogen synthesis regulation and facilitates studies of glycogen-related diseases.

Introduction

Glycogen is a branched polymer of glucose that functions as the primary energy store in eukaryotes. In its mature form, the glycogen particle can comprise up to ~50,000 glucose units that are rapidly utilized when glucose levels are low. Glycogen is stored predominantly in the muscle and liver cells, and to a lesser extent in other organs and tissues including kidney, brain, fat and heart[1].

Glycogen is synthesized through the cooperative action of three enzymes: glycogenin (GN), glycogen synthase (GS) and glycogen branching enzyme (GBE)[2]. GN initiates the process via auto-glucosylation of a conserved tyrosine residue, producing a primer glucose chain of 8-12 resides connected by α-1,4-linkages[3] (**Fig. 1a**). This glycogen initiating particle is further extended by GS after its recruitment by the GN C-terminus allowing the addition of glucose residues using α-1,4-linkages[4,5]. GBE introduces α-1,6-linkages every 6-8 residues to the growing glycogen molecule, thus creating the final globular structure containing GN at the centre[2,6] (**Fig. 1b**). Glycogen exists as a population of molecules with varying sizes (10-290 nm) in different tissues and species, although the importance of this variability is not well understood[1,7].

Glycogen synthesis and breakdown are tightly regulated processes, and thus dysregulation of the enzymes involved in glycogen metabolism contributes to glycogen storage diseases (GSDs), diabetes, neuroinflammation, neurodegeneration and muscle damage[1,8]. Excessive and/or abnormal glycogen is a common characteristic in most GSDs. Pompe disease (GSDII) is caused by deficiency of acid-α-glucosidase, resulting in accumulation of lysosomal glycogen and consequent lysosomal destruction and dysfunction[9]. Lafora disease is a fatal neurodegenerative condition, characterized by Lafora bodies that contain hyperphosphorylated and poorly branched, insoluble glycogen deposits[10]. In addition, loss of GS-GN interaction results in muscle weakness and cardiomyopathy[11].

Studies using mouse models have found inhibition of glycogen synthesis, particularly by reducing GS activity, to be beneficial for multiple GSDs[12-16] . To date there is no structure of the GS-GN complex and no structure of human GS. Since inhibition of GS activity is potentially beneficial for GSD patients, obtaining a human GS-GN structure and understanding how GS is regulated is instrumental in developing new therapeutics.

GN is found in two isoforms, GN1 and GN2, encoded by the *GYG1* and *GYG2* genes respectively. While *GYG1* is widely expressed, *GYG2* is restricted to the liver, pancreas and heart[17,18]. GN belongs to the GT8 family of glycosyltransferases, containing a glycosyl transferase A (GT-A) fold with a single Rossmann fold domain at the N-terminus, which is essential for binding of the glucose donor uridine diphosphate glucose (UDP-G)[19-21]. The C-terminus comprises a highly conserved region of ~34 residues (GN^{34}) which is the minimal targeting region for binding GS[5,22]. Other interaction interfaces have been suggested[23], but, further investigation into the full-length complex is required to precisely define any additional interaction interfaces. The area between the N-terminal catalytic domain and C-terminal GS binding motif is a linker region that is variable in sequence and in length (**Fig. 1c and Supplementary Fig. 1**).

GS is also found as two isoforms, GS1 and GS2, encoded by the *GYS1* and *GYS2* genes respectively. These are differentially expressed, with *GYS1* being expressed predominantly in skeletal muscle and most other cell types where glycogen is present, while *GYS2* is expressed exclusively in the liver[24-26]. Eukaryotic GS belongs to the GT3 family of glycosyltransferases with a GT-B architecture comprising an N-terminal and a C-terminal Rossmann fold domain, with an interdomain cleft that contains the active site[19,27]. GS is the rate limiting enzyme in glycogen biosynthesis and as such its activity is tightly regulated[28]. GS is inactivated by covalent phosphorylation at numerous N- and C-terminal sites (**Fig. 1c**), and is allosterically activated by glucose-6-phosphate (G6P) binding and/or dephosphorylation[2,29,30]. Human GS phosphorylation sites lie at the N-terminus (sites 2 and 2a) and C-terminus (sites 3a, 3b, 3c, 4, 5, 1a, 1b), and phosphorylation occurs in a hierarchical fashion, whereby the phosphorylation of a specific site is the recognition motif for subsequent phosphorylation[31-33] (**Fig. 1c and Supplementary Fig. 2**). How the metazoan GS is inhibited is not clear and while allosteric activation by G6P binding been described for the yeast GS paralogues[34] no structural information of the phosphorylated version of the enzyme exists.

The complex interplay between allosteric activation and inhibitory phosphorylation is not yet fully understood, at least in part because of the lack of structural data for the full GS-GN complex. Although a binary GS-GN complex was co-purified over 30 years ago[3], we have yet to confirm the stoichiometry of this complex and identify precisely how the two proteins cooperate to make glycogen.

Here, we report the structural and functional analysis of the full-length human GS-GN complex and the cryo-EM structure of phosphorylated human GS. The structure reveals that phosphoregulatory elements form a flexible inter-subunit “spike” region emanating from two

103 GS protomers, which help to keep GS in an inactive conformation via interactions of
104 phosphorylated Ser641 (site 3a) with arginine residues from GS regulatory helices, which we
105 have termed the arginine cradle. Moreover, low resolution maps of GN bound to GS reveal
106 two flexible GN dimers coordinating a GS tetramer, providing new insights into the
107 stoichiometry and the conformational plasticity of this enzyme complex. Collectively, these
108 results shed light on the regulation of glycogen biosynthesis and the inner workings of how
109 GS and GN cooperate to synthesize glycogen.
110
111 **Results**
112
113 **GS-GN forms an equimolar 4:4 complex**
114
115 To characterize the synthesis of glycogen by the GS-GN complex, we expressed and purified
116 human full length GS1 and GN1 in insect cells. Consistent with previous reports, co-
117 expression of GS with GN resulted in improved production yields over the expression of GS
118 alone[35,36]. Purification of the wild-type (WT) complex resulted in a highly glucosylated sample,
119 as evidenced by a smear by SDS-PAGE corresponding to glucosylated GN detected by
120 Coomassie stain, periodic acid-Schiff (PAS) staining and immunoblotting (**Fig. 1d and**
121 **Supplementary Fig. 3b and 3c**). In-gel protease digestion of different molecular weight
122 regions (encompassing mass ranges from 43-55 kDa, 55-72 kDa, 95-130 kDa and greater
123 than 130 kDa) combined with tandem mass spectrometry confirmed the presence of GN1 in
124 all these higher MW species (**Supplementary Data 1**). In addition, treatment of GS-GN
125 preparations with α-amylase (endo-α-1,4-d-glucan hydrolase) resulted in the disappearance
126 of the smeared bands revealing a single, sharp band migrating at the expected molecular
127 weight for GN1 (~37.5 kDa) and also absence of glucosylated species after PAS staining.
128 Thus, confirming that the smearing effect is due to glucosylation of GN (**Supplementary Fig.**
129 **3d**). Mutation of the GN auto-glucosylating tyrosine 195[37,38] to a phenylalanine (Y195F),
130 resulted in a non-glucosylated GN species, as shown by a single band for GN migrating at the
131 expected size (~37.5 kDa) detected by Coomassie stain and immunoblotting and absence of
132 glucosylated species after PAS staining (**Fig. 1e, Supplementary Fig. 3b and Fig. 1d**).
133
134 To determine the stoichiometry of the GS-GN complex, we first performed mass photometry
135 analysis of GS-GN and GS-GN(Y195F) mutant complexes, which enables mass
136 measurements of single molecules in solution. Mass photometry measurements of the GS-
137 GN(Y195F) complex showed a predominant species with an average molecular weight of 473
138 kDa, which is suggestive of a 4:4 stoichiometry (calculated mass of 485 kDa) (**Fig. 1f)**.

139 Analysis of the GS-GN(WT) sample identified a species with an average molecular weight of
140 534 kDa and the measured peak was broader than the non-glucosylated species (**Fig. 1f**).
141 While mass photometry measurements lack the resolution to ascertain the precise molecular
142 mass of heterogeneously glucosylated species, the observed increase in average molecular
143 mass and overall distribution of the WT complex when compared to the Y195F complex is
144 consistent with the observed higher molecular weight of WT GN1 glucosylated species (**Fig.**
145 **1d and Supplementary Fig. 3b**).

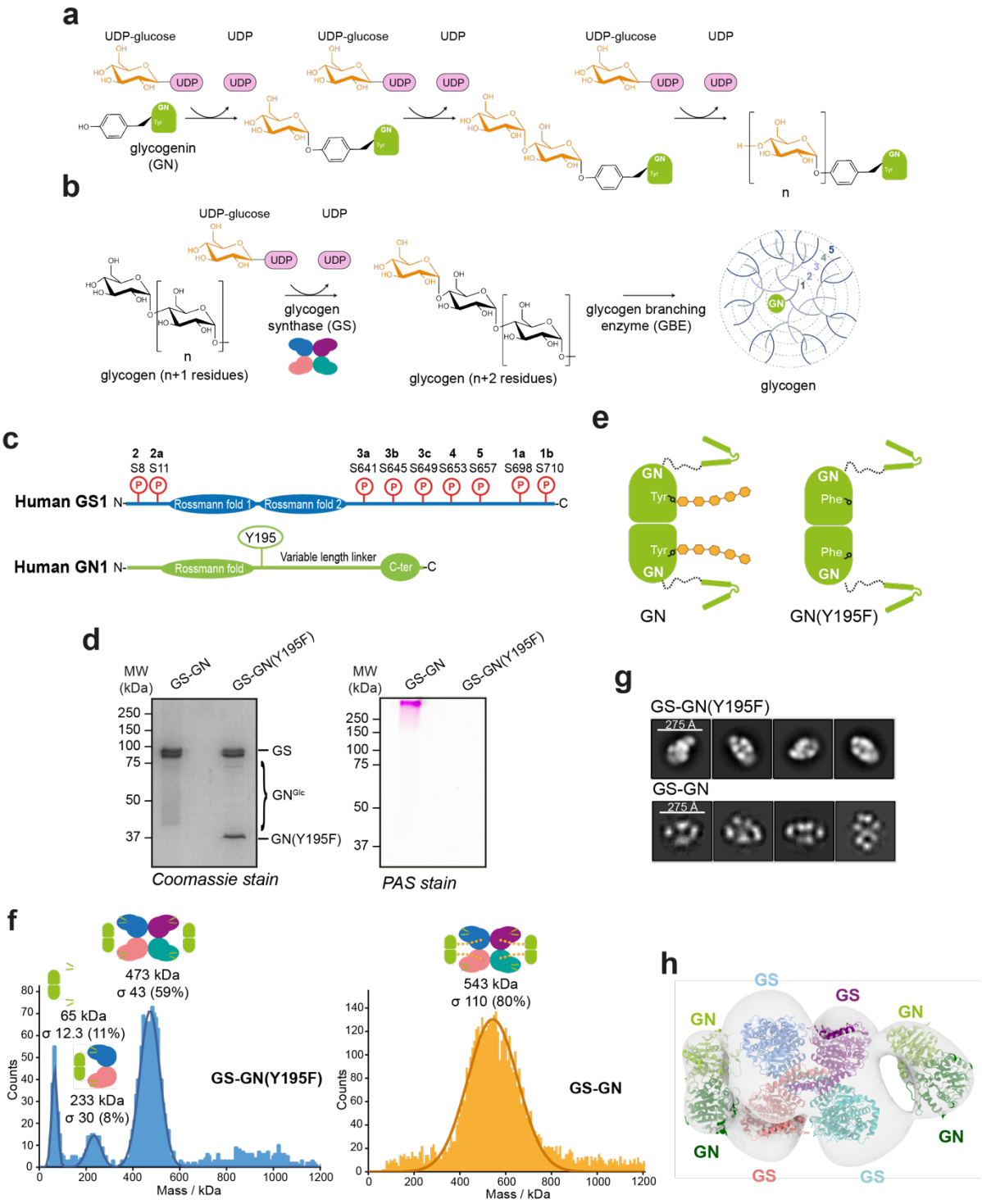

Fig. 1 Structural analysis of the full-length GS-GN complex

a Enzymatic reaction catalyzed by GN. **b** Enzymatic reaction catalyzed by GS and subsequent branching of glycogen by GBE. **c** Domain architecture of human GS (top) and GN (bottom). Known *in vivo* phosphorylation sites of GS are shown in red and are labelled with residue number and classical nomenclature (in bold). GN tyrosine 195 that becomes auto-glucosylated and mutated to a phenylalanine (Y195F) in this study is indicated. Not to scale. **d** SDS-PAGE analysis of GS-GN WT and Y195F complexes (left) and periodic acid-Schiff (PAS) staining of both complexes (right). **e** Cartoon representation of GN WT and Y195F. **f** Mass photometry of GS-GN(Y195F) (left) and WT complex (right). Expected stoichiometry for each peak is indicated. The percentage of particles contributing to each peak is shown in brackets. **g** Selected 2D class averages after negative-stain electron microscopy (nsEM) analysis of indicated GS-GN complexes. **h** nsEM final map (C1 symmetry at ~22 Å) is shown in transparent surface, with fitted human GN crystal structure (PDB ID 3T7O) and human GS cryo-EM structure (reported here).

146

147 To understand how GS and GN interact and to reveal the overall shape of the GS-GN complex
148 we performed negative stain electron microscopy (nsEM) of the WT and Y195F complexes.
149 2D class averages show two GN dimers, one on either side of a GS tetramer, for both WT and
150 mutant complexes (**Fig. 1g**). Final 3D maps for both complexes are consistent with the 2D
151 classes, and the reconstructed 3D EM density map can accommodate a GS tetramer flanked
152 by two GN dimers (**Fig. 1h**). This nsEM confirms a 4:4 stoichiometry and is consistent with
153 previous findings showing that GS can interact with four GN C-terminal peptides
154 simultaneously[4,5,17]. Surprisingly, GN dimers do not engage the GS tetramer in an identical
155 fashion, with one GN dimer tilted slightly towards GS and bringing it closer to one of the GS
156 subunits (**Fig. 1h**). Collectively, these results provide the first glimpse of the glycogen initiating
157 particle, where two GN dimers can engage a single GS tetramer.
158
159 **Phosphorylated human GS is in the inactive state**
160
161 GS is regulated by both allosteric activation by G6P and inhibition via phosphorylation of its
162 N- and C-terminal tails[2] (**Fig. 1c**). Mechanistic and structural studies of yeast GS have
163 elegantly dissected its allosteric activation by G6P[30,34]. However, GS structures to date were
164 from protein preparations produced in bacterial expression systems and thus could not provide
165 insights into the phospho-regulatory apparatus. Our GS-GN preparations are from eukaryotic
166 expression systems and therefore provide an opportunity to study the inactive GS form. We
167 confirmed that GS was phosphorylated at sites 2 (S8) and 3a (S641) and the enzyme
168 preparation was inactive unless stimulated by G6P or dephosphorylation (**Fig. 2a and 2b**).
169 Protein phosphatase 1 (PP1) and lambda protein phosphatase (lambda PP) treatment
170 resulted in faster migration of GS by SDS-PAGE and also a reduction in signal detected by
171 specific phosphorylation site antibodies (**Fig. 2a and Supplementary Fig. 4a**). Notably, we
172 see only minor dephosphorylation of the GS-GN(Y195F) complex with PP1 alone, which was
173 associated with a 5-fold increase in basal activity (-G6P) (**Fig. 2a and 2b**). We observed a 15-
174 fold increase in basal activity when GS is dephosphorylated by both PP1 and lambda PP (**Fig.
175 2b**). The phosphorylated and dephosphorylated GS forms were similarly active after addition
176 of G6P (**Fig. 2b**), which is consistent with studies using GS from endogenous sources[39,40].

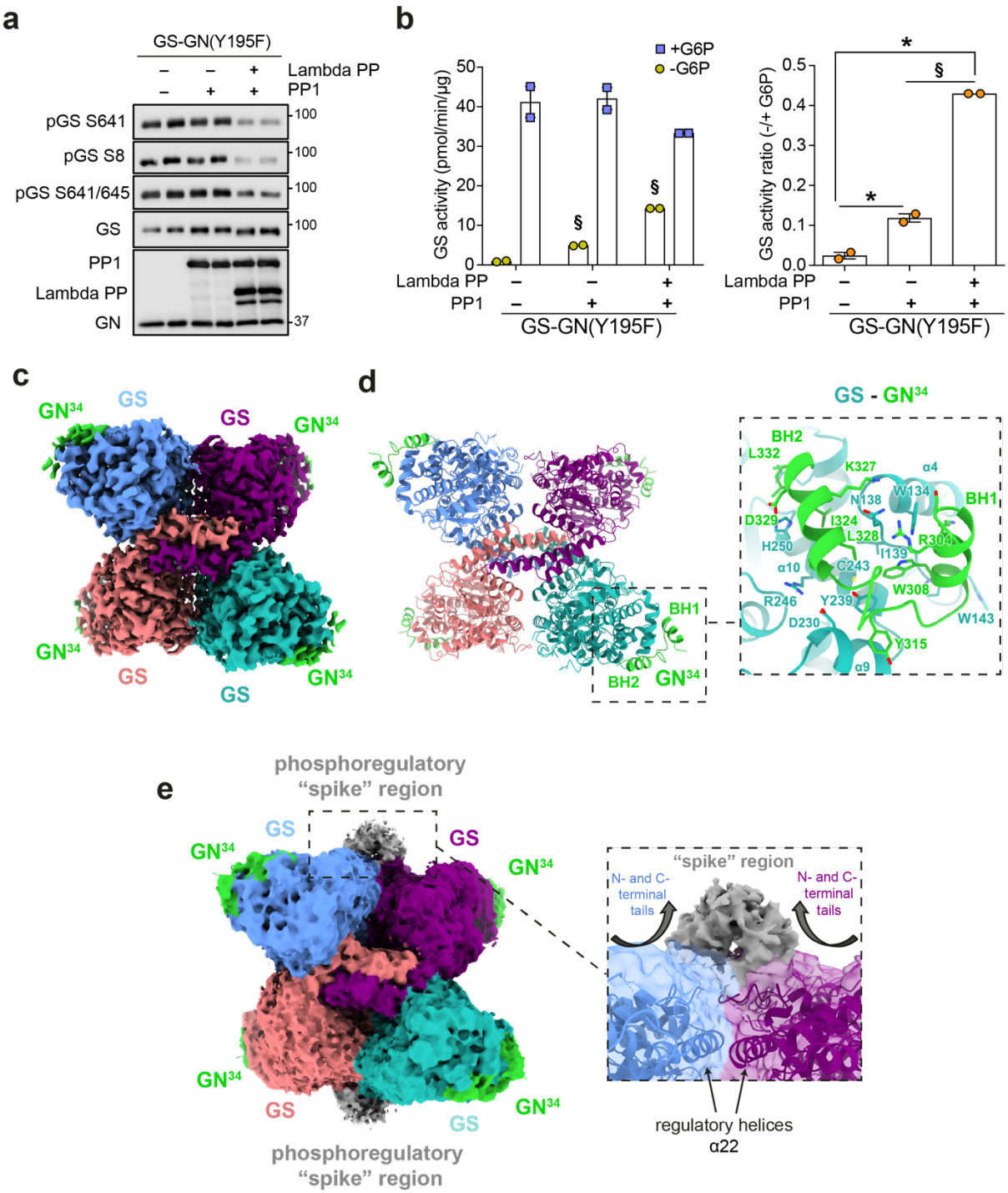

Fig. 2 Cryo-EM structure of human GS-GN^{34} complex
a Immunoblot for the indicated human GS phosphorylation sites and total GS. **b** Activity of GS-GN(Y195F) with and without the addition of lambda protein phosphatase (lambda PP) and protein phosphatase 1 (PP1) (left) and -/+ G6P activity ratio (right). Upon G6P saturation, GS reaches similar activity levels regardless of phosphorylation state. Data are mean +/- S.E.M. from n=2 and representative of two independent experiments. One-way analysis of variance (Tukey's post hoc test); §= p<0.05, +PP1 vs. +PP1+lambda PP (-G6P) (left). *= –PP1–lambda PP vs. +PP1 vs. +PP1+lambda PP, §= +PP1 vs. +PP1+lambda PP (right). **c** 2.6 Å cryo-EM map of the GS tetramer coloured by corresponding chain. Density corresponding to the GN^{34} C-terminal region is shown in green. **d** Human GS-GN^{34} cartoon model shown in ribbons coloured by corresponding chain (left). Interaction between GS and GN^{34} (right). **e** Unsharpened cryo-EM map shown at a lower threshold to visualise the "spike" region depicted in grey (left). The N- and C-terminal tails of two protomers converge and form the "spike" region (right).

177

178 To better understand the extent of phosphorylation we used tandem mass spectrometry
179 (MS/MS) after proteolysis with either trypsin, chymotrypsin or elastase to map the
180 phosphorylation sites of human GS. This resulted in a sequence coverage of 97%, which is
181 higher than the 73%[35] and 65%[36] sequence coverage achieved in previous studies (**Table 1**
182 **and Supplementary Fig. 4b**). Our analysis identified canonical sites 2, 3a, 3b, 4 and 5 (S8,
183 S641, S645, S653, S657), and also non-conventional sites (S412, S652, S727, S731). In
184 addition, we could detect human GS site 2 (S8) phosphorylation by mass spectrometry for the
185 first time in a recombinant enzyme preparation. Together, these results show that expression
186 in insect cells is sufficient to achieve phosphorylation at multiple inhibitory sites and to provide
187 suitable enzyme preparations to study inactive GS.
188
189 **Table 1:** Summary of GS phosphorylation site analysis. Peptide modifications show either
190 phosphorylation (P) or oxidation (O). PhosphoSite Plus (web-based bioinformatics resource)
191 was used for comparison of our results with previous literature. LTP and HTP refer to low
192 throughput site determination (methods other than mass spectrometry) and high throughput
193 analysis (mass spectrometry only), respectively[41].

Site	Sequence	Peptide modifications	ptmRS Score	MASCOT score	Enzyme	PhosphoSite: LTP	PhosphoSite: HTP
S8	PLNRTLsMS	S7(P)	S7: 100	40	Elastase	15	1
S8	PLNRTLsMS	S7(P); M8(O)	S7: 100	31	Elastase	15	1
S8	sMSSLPGLEDW	S1(P)	S1: 99.71	13	Chymotrypsin	15	1
S412	ESLLVGsLPDMNKMLDKEDF	S7(P)	S7: 100	31	Chymotrypsin	-	17
S412	ESLLVGsLPDMNKML	S7(P); M11(O); M14(O)	S7: 100	23	Chymotrypsin	-	17
S641	QGYRYPRPAsVPPSPS	S10(P)	S10: 99.99	20	Elastase	32	30
S641 & S645	QGYRYPRPAsVPPsPS	S10(P); S14(P)	S10: 100; S14: 100	24	Elastase	(645) 21	(645) 39
S652	RHsSPHQSEDEEDPRNGPL	S3(P)	S3: 99.78	34	Elastase	-	15
S652 & S653 & S657	RHssPHQsEDEEDPRNGPL	S3(P); S4(P); S8(P)	S3: 100; S4: 100; S8: 100	19	Elastase	(653) 13	(653) 27
S652 & S657	RHsSPHQsEDEEDPRNGPL	S3(P); S8(P)	S3: 99.67; S8: 100	53	Elastase	(657) 14	(657) 50
S727	RNSVDTATSSSLSTPSEPLsPTSSLGEER	S20(P)	S20: 100	66	Trypsin	1	22
S727	STPSEPLsPTSSL	S8(P)	S8: 99.63	20	Chymotrypsin	1	22
S731	STPSEPLSPTSsLGEERN	S12(P)	S12: 99.79	73	Chymotrypsin	-	6
S731	TPSEPLSPTSsL	S11(P)	S11: 100	22	Elastase	-	6
S727 & S731	NSVDTATSSSLSTPSEPLsPTSsLGEER	S19(P); S23(P)	S19: 100; S23: 99.52	60	Trypsin	see above	
S727 & S731	STPSEPLsPTSsLGEERN	S8(P); S12(P)	S8: 100; S12: 100	42	Chymotrypsin	see above	

194
195
196 **<u>High resolution structure of human GS</u>**
197
198 Previous attempts to crystallise full-length GS in complex with full-length GN were
199 unsuccessful[22] leading us to pursue structural analysis using cryo-electron microscopy (cryo-
200 EM). NsEM indicated that the position of each GN dimer is different suggesting flexibility of
201 GN in the complex (**Fig. 1g and 1h**). Cryo-EM analysis of the GS-GN(Y195F) complex
202 confirmed this GN flexibility as evidenced from the lack of GN signal in 2D class averages

203 (**Supplementary Fig. 5a**) and subsequent 3D maps. Although we could detect the presence
204 of GN after data processing without the application of symmetry averaging (**Supplementary**
205 **Fig. 6c**), it was not possible to trace the connecting residues between the GN globular domain
206 and the C-terminal GN^{34} region that binds GS. To gain a higher resolution structure for the
207 human GS, we applied D2 symmetry and achieved a global resolution of 2.6 Å (EMDB-14587)
208 (**Fig. 2c, Supplementary Fig. 5 and Supplementary Table 1**). The 3D reconstruction
209 revealed a tetrameric arrangement of human GS in agreement with the crystal structures of
210 the *C. elegans* GS and yeast GS enzymes, with root mean square deviation (RMSD) values
211 of 1.1 Å (between 484 Cα atom pairs) and 0.9 Å (between 522 Cα atom pairs) respectively
212 (**Fig. 2d, Supplementary Fig. 7a and 7b**). Structural analysis of the human GS-GN(WT)
213 complex revealed a 6 Å map of the GS tetramer and comparing this to the GS structure from
214 human GS-GN(Y195F) complex reveals no differences at this resolution (**Supplementary**
215 **Fig. 6d and 6e**).
216
217 Density for the C-terminal GS interacting region of GN allows for model building of residues
218 300-332 (human GN^{34}). Four GN peptides bind to the GS tetramer, and these residues form
219 a helix-turn helix, where the first helix is denoted binding helix 1 (BH1) and the second as BH2
220 (**Fig. 2d)**. This is consistent with the *C. elegans* GS-GN^{34} crystal structure[22], with an RMSD
221 value of 0.8 Å (between 30 Cα atom pairs) (**Supplementary Fig. 7c**). The interaction interface
222 between human GS, namely α4, α9 and α10, and human GN^{34} is mediated by a combination
223 of hydrophobic and hydrogen bonding interactions and is consistent with the interactions
224 observed for GS-GN^{34} from *C. elegans*[22] (**Fig. 2d and Supplementary Fig. 7c**).
225
226 **<u>Mechanism of GS inactivation</u>**
227
228 A unique feature of metazoan GS is that both N- and C-terminal tails are phosphorylated, but
229 the mechanism by which they participate in enzyme inactivation has remained elusive. We
230 were able to build a model for the N-terminus starting from residue 13, and of the C-terminus
231 up to residue 625, and then from 630-639 (chain A/C) and 630-642 (chain B/D), that could
232 help understand the mechanisms of GS inactivation (PDB 7ZBN). The N- and C-terminal tails
233 of each GS protomer lie almost parallel to each other, and travel side by side along the GS
234 tetrameric core to reach the centre (**Fig. 3a**, right panels). Here, the C-terminal tail (chain A)
235 meets the C-terminal tail from an adjacent GS protomer (chain B), which has travelled from
236 the opposite direction (**Fig. 3a,** right panels). A 2.8 Å cryo-EM map of GS generated without
237 the application of D2 symmetry averaging (EMDB-14587) (**Supplementary Fig. 6a and 6b**),
238 suggests that one C-terminal tail disengages with the GS core earlier than the other C-terminal

239 tail from the adjacent chain. The C-terminal tail from chain B continues to travel further across
240 the regulatory helices than chain A, prior to traversing away from the core (**Fig. 3a**). This
241 allows chain B to engage with the regulatory helices α22, specifically phosphorylated S641
242 interacting with residues R588 and R591, which come from two GS protomers to form a
243 positively charged pocket we have termed the "arginine cradle" (**Fig. 3a and Supplementary**
244 **Fig. 7d**). This is consistent with our phosphorylation mapping and immunoblotting data
245 showing S641 is phosphorylated in our preparations (**Table 1, Supplementary Fig. 4b and**
246 **Fig. 2a)**.
247
248 S641 is a major phosphorylation site involved in the regulation of GS activity[40,42], and
249 interaction of pS641 with the arginine cradle in helix α22 shows the mechanism of inactivation
250 of human GS through constraining the GS tetramer in a "tense state". This interaction therefore
251 provides a crucial activity switch mechanism from a tense (phosphorylated) state to a relaxed
252 (G6P-bound) state[30]. The involvement of helices α22, which also interact with G6P via the
253 nearby arginine residues R582 and R586[30] (**Supplementary Fig. 8a**), provides a possible link
254 between G6P-binding and its ability to override inactivation by phosphorylation.
255
256 The Rossmann fold domains of human GS were predicted to a high level of accuracy by
257 AlphaFold[43] (RMSD 1.0 Å between 575 Cα atoms), although the position of the N- and C-
258 terminal tails does not agree entirely (**Supplementary Fig. 8c**). However, the position of S641
259 is consistent and overlays well with the phospho-S641 modelled in our cryo-EM structure
260 (**Supplementary Fig. 8d**). This suggests that a Ser641 interaction with the arginine cradle
261 may also be possible in the non-phosphorylated state, although the negative charge on the
262 phosphate group would naturally provide stronger interactions with the positively charged
263 arginine cradle.
264

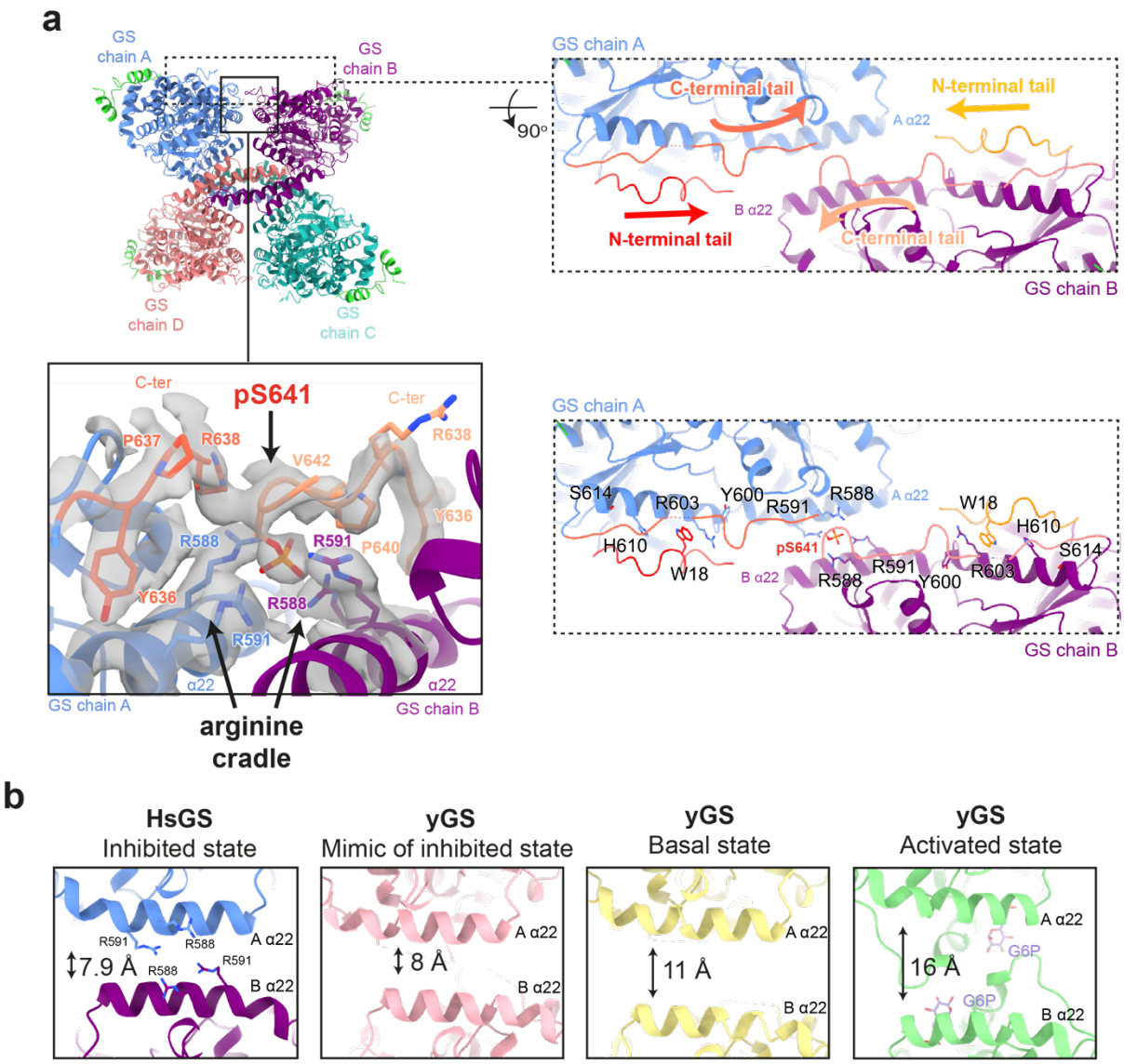

Fig. 3 The phosphoregulatory region of human GS
a Human (Hs)GS-GN[34] structure shown in ribbons (top left). The N- and C- terminal tails of one GS protomer (chain A) lie next to one another and move towards the adjacent protomer, meeting the N- and C-terminal tails from chain B. Arrows indicate continuation of cryo-EM density (top right). Electron density (C1 symmetry) for phosphorylated S641 (pS641) interacting with R588 and R591 on the regulatory helices α22 (bottom left). Residues that are interacting with the N- and C-terminal tails that are mutated in this study are shown (bottom right). **b** Comparison of distances between regulatory helices of adjacent monomers of HsGS (reported here), low activity inhibited mimic (PDB ID 5SUL), basal state (PDB ID 3NAZ) and G6P activated (PDB ID 5SUK) yeast crystal structure. Quoted distances were measured from Cα of Arg591 (chain A) and -Cα of Arg580 (chain B) of HsGS and corresponding yeast (yGS) residues.

265

266 **<u>GS contains a dynamic "spike" region</u>**

267

268 Notably, the EM structures maps show density for an inter-subunit region that extends from
269 the N- and C- termini of two adjacent GS protomers. These N- and C-termini contain the GS
270 phosphoregulatory apparatus which meet and traverse away from the GS core (**Fig. 2e**).

271 Analysis of this ~25 kDa region by focussed 3D classification (without applying symmetry)
272 reveals that the region is highly flexible, as seen by the various different conformations
273 (**Supplementary Fig. 5f and 5g**). Interestingly, these "spike" regions were present in all the
274 refined classes, and suggests that GS exists as a continuum of structures with a core inactive
275 tetramer and "dynamic spikes" buttressed on either side, thus preventing GS from adopting
276 an open, active conformation.
277
278 To explore the flexibility and mobility of GS, we performed 3D variability analysis[44] using
279 cryoSPARC[45]. The dynamic movements of the "spike" region and concurrent movements of
280 the GS tetramer are highlighted in Movie S1. Consistent with the focussed 3D classification,
281 the "spike" is highly mobile, whereas only slight flexibility was observed within each GS
282 protomer. This suggests a role of the "spike" region in constricting a tense state of the GS
283 tetramer, and subsequently contributing to the GS regulation.
284
285 **Cross species comparison of GS structures**
286
287 When comparing human GS to previous crystal structures of yeast GS, the distance between
288 regulatory helices (α22) in adjacent monomers changes according to the activity state of GS
289 (**Fig. 3b**). In the phosphorylated human GS structure, helices α22 lie 7.9 Å apart when
290 measuring Cα-Cα distances from Arg591 on chain A and Arg580 on chain B (**Fig. 3b**). A
291 similar measurement of the corresponding residues in the yeast proteins shows that helices
292 α22 are furthest apart, at 16 Å, when G6P is bound and GS is in its high activity state, and
293 this translates into better access for accepting the substrate[30,34]. When no G6P is bound and
294 there is no phosphorylation, GS is in the basal state and the helices lie 11 Å apart[30]. In a yeast
295 GS structure of a mimic of the inhibited state, where residues R589 and R592 were mutated
296 to Ala and GS was produced in bacteria, the helices are closest together at 8 Å[34]. This is
297 similar to the phospho-human GS, where phosphorylation appears to contribute to the closing
298 of the regulatory helices constraining the GS tetramer and thus locking it in a tense, inactive
299 state (**Fig. 3b).**
300
301 The position of the extreme N-terminus is noticeably different in human and *C. elegans* GS
302 structures compared to yeast (**Supplementary Fig. 7e**). The majority of the first β-sheet in all
303 structures is in a similar orientation, however human residues before 26 (residue 7 in yeast)
304 move in the opposite direction to yeast (**Supplementary Fig. 7e**). This positioning of the
305 human GS N-terminus is directed towards the regulatory helices α22. Previous structural
306 investigation of *C. elegans* GS-GN[34] suggested a hypothesis where phosphorylation could

307 enable the N-terminus to engage with regulatory helices, as the N-terminus is also situated
308 towards the regulatory helices[22] (**Supplementary Fig. 7e**). Our structure of the human,
309 phosphorylated enzyme supports this hypothesis, although the current density does not allow
310 model building before residue 13. However, using LAFTER[46] denoised maps to aid model
311 building and electron density interpretation, some density for the N-terminus is present next
312 to the regulatory helices, near to R579 and R580. This suggests that perhaps the N-terminal
313 phosphorylation sites can also interact with the regulatory helices and/or nearby residues (**Fig.
314 3a and Supplementary Fig. 7f**).
315
316 Comparisons between human, *C. elegans* and yeast GS structures are consistent with the
317 human structure in the inactive state. Each human GS protomer shows a closed conformation
318 of its active site, and a regulatory loop, that only becomes ordered upon G6P binding, is
319 disordered in the human structure (**Supplementary Fig. 8b and 8a**). Previous studies have
320 suggested that phosphorylated tails may be able to engage the G6P binding site and directly
321 compete with G6P. However, our EM density maps show no extra density within the G6P
322 binding site (**Supplementary Fig. 8a**). Thus, we see no evidence to support the hypothesis
323 that the phosphorylated tails interact with residues lining the G6P pocket to directly compete
324 with G6P binding. Instead, we posit that the phosphoregulatory regions indirectly affect G6P
325 binding by constraining the opening and closing of the GS tetramer. Collectively, our structural
326 analyses support a model by which phosphorylated N- and C-terminal tails inhibit the GS
327 tetramer by constraining a tense conformation through inter-subunit interactions.
328
329 **<u>Dislodging the GS phosphoregulatory region</u>**
330
331 Due to the flexibility evident in the N- and C-terminal tails, we were unable to build
332 phosphorylated residues in the cryo-EM map other than phospho-S641. However, we can see
333 the beginning of the flexible phosphoregulatory "spike" region and residues from the GS "core
334 tetramer" which interact with this regulatory region (**Fig. 3a,** bottom right panel). To investigate
335 the relationship between allosteric regulation and inhibitory phosphorylation and elucidate the
336 mechanism of inactivation, we mutated residues in GS that contact the beginning of the
337 phosphoregulatory region. We selected residues which are not involved in G6P binding and
338 mutated these in order to "dislodge" the regulatory tails (**Fig. 3a and Supplementary Fig. 8e**).
339 If the phosphorylated tails are indeed holding GS in an inactivated state, weakening the
340 interaction between the core tetramer and the N- and C-termini inhibitory regions should
341 create an enzyme with higher basal activity in comparison to the WT. Consistent with our
342 hypothesis, we observed a marginal increase in basal (-G6P) GS activity in R588A+R591A,
343 Y600A, R603A, H610E and W18A mutants, that was reflective of the phosphorylated state at

residues S8, S641 and S645 (**Fig. 4a and 4b**). These mutants were unaffected in terms of GN co-purification and with the exception of R588A+R591A mutant, they had similar melting (T_m) profiles and oligomeric state to the WT GS complexes (**Supplementary Fig. 3e, Fig. 4c, Supplementary Fig. 9**). All mutants except Y600A could still be activated to similar levels to the WT upon addition of G6P (**Fig. 4a)**.

Upon addition of PP1 and lambda PP, the GS mutants R588A+R591A, R603A and W18A were more robustly dephosphorylated at S641 and S8 than WT GS (**Fig. 4d**), suggestive of increased exposure of the phospho-tails to phosphatases. For the W18A mutant, this dephosphorylation by both lambda-PP and PP1 resulted in over a 20-fold increase in basal activity, and also an approximately 3-fold increase in comparison to WT GS (**Fig. 4e**). The GS R603A-GN(Y195F) mutant has a basal activity similar to WT GS upon dephosphorylation. However, the robust dephosphorylation at S641 and S8 in GS R588A+R591A was not associated with an increase in activity (**Fig. 4e**). As described above, R588 and R591 lie on the regulatory helices and are also involved in inter-subunit interactions and form the arginine cradle that interacts with phospho-S641 (**Fig. 3a**). In addition, we noticed some dissociation of the GS R588A+R591A double mutant complex in mass photometry (**Supplementary Fig. 9c**). Therefore, the role of these residues in stabilising the GS tetramer may be the cause for the lack of rescue of activity upon dephosphorylation (**Fig. 4e**). Moreover, dephosphorylated GS had a markedly lower T_m (48 ºC) than WT or mutant GS (**Fig. 4c)** supporting the idea that phosphorylation of the “spike” regions strengthens the inter-subunit interactions within the tetramer and holding the enzyme in the “tense” conformation.

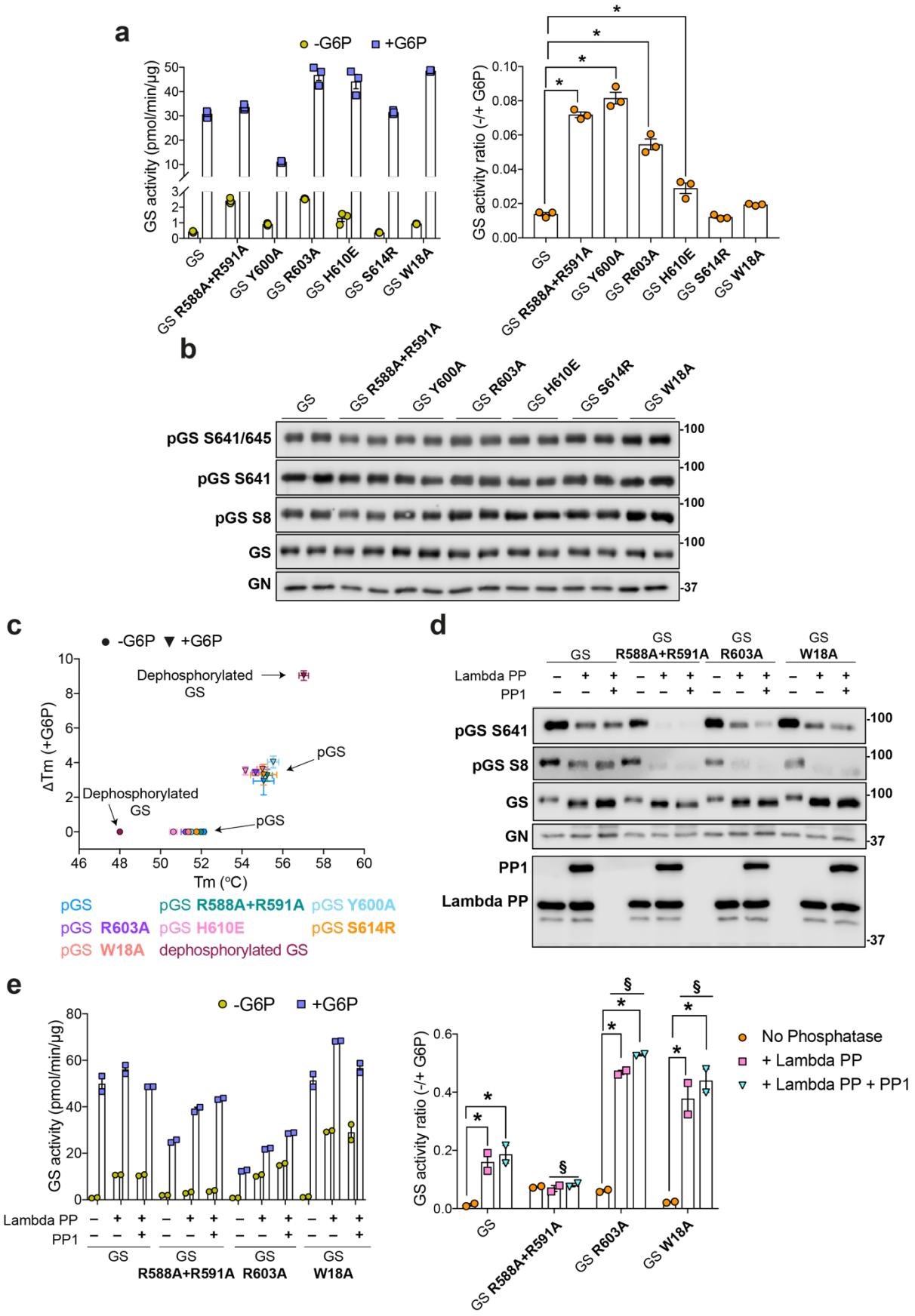
a
-G6P
+G6P
GS activity (pmol/min/µg)
GS activity ratio (-/+ G6P)
GS
GS R588A+R591A
GS Y600A
GS R603A
GS H610E
GS S614R
GS W18A
b
pGS S641/645
pGS S641
pGS S8
GS
GN
c
-G6P
+G6P
ΔTm (+G6P)
Tm (°C)
Dephosphorylated GS
pGS
pGS R588A+R591A
pGS Y600A
pGS R603A
pGS H610E
pGS S614R
pGS W18A
dephosphorylated GS
d
Lambda PP
PP1
pGS S641
pGS S8
GS
GN
PP1
Lambda PP
e
-G6P
+G6P
GS activity (pmol/min/µg)
GS activity ratio (-/+ G6P)
No Phosphatase
+ Lambda PP
+ Lambda PP + PP1

Fig. 4 Dislodging the GS phosphoregulatory region increases basal activity and increases accessibility for phosphatases
a Activity of GS WT and indicated mutants in the GS-GN(Y195F) complex in the presence and absence of G6P (left) and -/+ G6P activity ratio (right). Data are mean +/- S.E.M from n=3 and representative of two independent experiments. One-way analysis of variance, (Tukey's post hoc test); *= $p<0.05$ **b** Western blot for human GS phosphorylation sites S641/645, S641, S8, and total GS and GN. **c** Melting temperature (T_m) of GS WT and mutants in the GS-GN(Y195F) complex. Changes in melting temperature upon addition of 12.5 mM G6P ($\Delta T_m = T_m^{+G6P} - T_m^{-G6P}$). Data are mean +/- S.E.M from n=3 experiments carried out in technical duplicates (dephosphorylated GS) and triplicates (WT and mutant GS). **d** Western blots of GS WT and mutants in the GS-GN(Y195F) complex after dephosphorylation with PP1 and/or lambda protein phosphatase (lambda PP). **e** Activity of phosphorylated and dephosphorylated GS WT and indicated mutants (left) and -/+ G6P activity ratio (right). Data are mean +/- S.E.M from n=2 and representative of two independent experiments. Two-way analysis of variance (Tukey's post hoc test); $p<0.05$ * = within groups, § = between groups: WT GS+lambda PP or +lambda PP+PP1 vs mutant GS +lambda PP or +lambda PP+PP1.

Discussion

For many decades human GS has remained elusive and resisted efforts for structural determination and characterization. Here, we provide structural and biochemical analysis of phosphorylated human GS in the full-length GS-GN complex. NsEM maps reveal two GN dimers binding to a GS tetramer, explaining the conformational plasticity of this octameric enzyme complex and the inner workings of how GS-GN cooperate to initiate glycogen synthesis (**Fig. 1 and Fig. 5**). The two GN dimers neighbouring a GS tetramer do not interact in an identical manner, with one GS dimer tilted closer towards GS in comparison to the other (**Fig. 1h**). This observed flexibility of GN may be aided by the variable length linkers connecting the catalytic domain and the C-terminal GN[34] region that anchors GS. The precise functional relevance of this movement is yet to be explored, however the linker length was shown to govern glycogen particle size and molecular weight distribution *in vitro*[22]. Thus, the ability for GN to interact flexibly with GS may facilitate the wide range of size and distribution of glycogen particles seen in multiple species and tissues[4].

Our human GS structure revealed phosphorylated S641 (site 3a) interacting with the regulatory helices α22. The electrostatic interactions between phospho-S641 and the arginine cradle could be strengthening the interaction between two GS protomers, thus constraining the GS tetramer and leading to an inactive enzyme (**Fig. 3a and 5**). Our structure also suggests a role for the N-terminal phosphorylation sites S8 and S11 (sites 2 and 2a) in the mechanism of human GS inactivation, as they presumably lie close to R579 and R580 on the regulatory helices (**Supplementary Fig. 7e and 7f**). Although model building before residue 13 was not possible, our analyses highlight an essential role for α22 in GS inhibition, specifically residues R579, R580, R588 and R591. This is consistent with previous studies

394 showing that both N- and C- phosphorylation is required for inhibition of rabbit GS, as well as
395 there being a significant role of site 3a and site 2/2a[23,42]. The role of the arginine cluster
396 (residues 579-591, on the α22 helices) in GS regulation was investigated in yeast orthologues,
397 revealing a role in G6P activation and suggesting a potential role in phosphorylation
398 dependent inactivation[30,34,47,48]. Our inhibited human GS structure confirms that helix α22 is
399 crucial for the phosphorylation dependent inactivation of GS, revealing that the same helix
400 α22 is involved in both allosteric activation[30] and covalent inhibition (**Fig. 3 and Fig. 5**).
401
402 GS phosphorylation sites lie outside of the catalytic core and within the N- and C- terminal
403 tails (**Fig. 1c and Supplementary Fig. 2**). A comparison of human, *C. elegans* and yeast
404 structures reveals considerable differences in the position of the tails (**Supplementary Fig.**
405 **7e**). In human GS, the C-terminus is responsible for most of the observable interactions with
406 helix α22 via R588 and R591 residues, however, these residues are not conserved in *C.*
407 *elegans* (**Supplementary Fig. 2**), perhaps explaining the positional differences between
408 human and *C. elegans* GS tails. Interestingly, S641 (site 3a) is also not conserved in *C.*
409 *elegans* GS, suggesting an evolutionary divergence, and hinting at additional mechanisms for
410 *C. elegans* GS inactivation where the N-terminus interacts with helix α22. This potential
411 exchange of interactions between N- and C-termini suggests a functional redundancy between
412 the multiple phosphorylation sites.
413
414 The non-identical engagement of the C-terminal tails and the proximity of the N-terminus to
415 the regulatory helices, as well as the flexibility of the "spike" region indicates coordination
416 between the N- and C- termini of a single GS protomer, as well as between protomers (**Fig.**
417 **3a and Supplementary Fig. 7f and 5g**). Having one tail buttressed against the regulatory
418 helix and the other steering away from the core may allow interchanging of the tails based on
419 their level of phosphorylation, perhaps explaining why multiple phosphorylation sites are
420 required. It may also aid/allow rapid dephosphorylation of GS, leading to an increase in GS
421 activity and thus promoting glycogen synthesis (**Fig. 5**).
422
423 Elucidating the role of the inter-subunit domain that house the phosphorylation sites, through
424 mutations that weaken the interactions between the core tetramer and the "spike" regions,
425 resulted in basal activity equal to or higher than the WT, yet retaining activation by G6P (**Fig.**
426 **4a**). The GS Y600A mutant was not activated by G6P to the same extent as WT (**Fig. 4a**),
427 and although Y600 does not directly bind to G6P, UDP or sugars[30,49,50], it is possible that this
428 hydrophobic residue is important for interdomain movements which are required for full GS
429 activation.

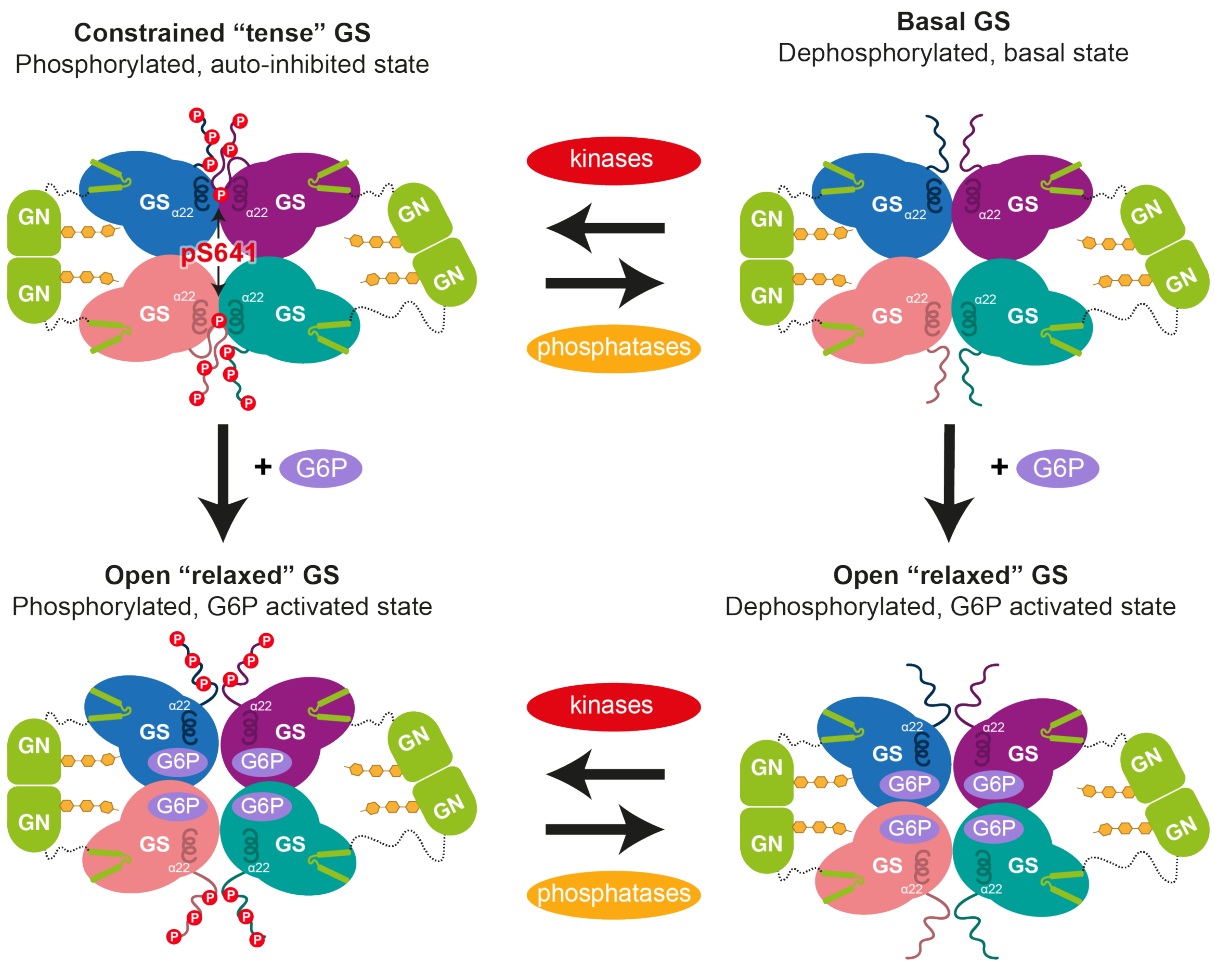

Fig. 5 GS and GN cooperate to synthesize glycogen
Glucose is converted into glycogen through the action of glycogenin (GN), glycogen synthase (GS) and glycogen branching enzyme (GBE). GN interacts with GS to feed the initial glucose chain into the GS active site for elongation. GS is regulated by allosteric activation and inhibitory phosphorylation. Phospho-S641 (pS641) from one C- terminal tail interacts with the regulatory helices α22 to cause enzyme inhibition. This can be relieved by G6P, with or without phosphatases, to reach a high activity state. Kinases can phosphorylate GS to inhibit the enzyme.

Dephosphorylation of the GS-GN(Y195F) complex resulted in an increase in basal activity, yet there is little difference in the high activity (G6P-bound) state between phosphorylated and dephosphorylated complexes (**Fig. 2a and Fig. 4a**). This is in accordance with previous studies that demonstrate that G6P can overcome inhibition by phosphorylation and restore full activity[2]. C-terminal mutants R588A+R591A and R603A and the N-terminal W18A mutant were more easily dephosphorylated than WT (**Fig. 4d**) suggesting that dislodging of the phosphoregulatory region leads to phosphorylation sites being more accessible to phosphatases.

441 The robust dephosphorylation of GS R588A+R591A did not result in an increase in basal
442 activity (**Fig. 4d and 4e**), which mirrors previous results in yeast[34]. The analogous mutations
443 were used in yeast GS resulting in low basal activity, yet it could still be fully activated by
444 G6P[34]. It was proposed that these residues in the regulatory helix are essential for keeping
445 GS in a "spring loaded" intermediate state, and thus charge neutralization by mutation of
446 arginine to alanine leads to the "tense" inactive state[34]. Our activity data agree with this as we
447 don't see an increase in basal activity despite dephosphorylation at S641 and S8, although
448 we do see a marginal difference between this mutant and WT in the phosphorylated state
449 (**Fig. 4a and 4e**). However, it is important to note that we also see some complex dissociation
450 with the R588A+R591A mutant as evidenced by a larger dissociated complex peak in mass
451 photometry (**Supplementary Fig. 9c**). It is possible that the dephosphorylated R588A+R591A
452 mutant is also unstable and dissociates more easily than the phosphorylated mutant, resulting
453 in a less active preparation.
454
455 Mutations of human GS1 and GS2 are common in glycogen storage diseases, and cluster
456 within pockets of GS, affecting UDP-G, G6P and sugar binding. Some mutations affect the
457 interaction between GS and GN[34], consistent with the requirement of this interaction for
458 glycogen synthesis[22]. The structure presented here will therefore provide a valuable resource
459 to understand disease mutations. In addition, this new structure and increased understanding
460 of GS regulation facilitates GS studies and its relevance in GSD, particularly Pompe and
461 Lafora diseases where a reduction of glycogen levels could be beneficial[12-16] . The high
462 resolution achieved here (2.6 Å) would undoubtedly be beneficial in efforts to design GS
463 inhibitors that block G6P, substrate binding and/or GS-GN[34] interaction.
464
465 GS has evolved a mechanism by which the phosphorylated N- and C-terminal "spike" regions
466 hold GS in an inactive conformation that is relieved by dephosphorylation and/or G6P binding.
467 We propose that the dynamic nature of these regulatory regions provides a functional
468 redundancy mechanism and serves the purpose of exposing phosphorylated residues to
469 phosphatases, thus allowing a "tuneable rheostat" instead of an on/off switch for regulating
470 GS activity. Collectively, our analyses of the human GS-GN enzyme complexes reveal
471 important mechanistic and structural details that could improve our understanding of GSDs.
472
473
474
475
476

477 **Materials and Methods**

478

479 **Materials**

480 Total GN antibody (S197C, third bleed) was obtained from MRC-PPU Reagents and Services.
481 Total GS (#3898) and p-GS S641 (#47043) antibodies were from Cell Signaling Technologies.
482 p-GS S641/S645 (#07-817) is from MerckMillipore. Affinity-purified p-GS S8 antibody
483 (YZ5716) was custom-generated by (YenZym Antibodies Brisbane, CA, USA) by
484 immunisation with a combination of phosphorylated peptides of the mouse GS1 (residues 2-
485 14: PLSRSL-*S-VSSLPG-Ahx-C-amide, in which the prefix * denotes the phosphorylated
486 residue) and human GS1 (residues 2-14: PLNRTL-*S-MSSLPG-Ahx-C-amide). Ahx and
487 Cysteine (C) were added at the C terminal of the antigen peptides as linker/spacer and for
488 conjugation to carrier protein, respectively. Antibody validation is shown in Supplementary Fig.
489 4c. Secondary antibodies (#711-035-152 and #713-035-147) were obtained from BioRad.
490 Glucose-6-phosphate (G6P) (#10127647001) is from Roche. All other chemicals if not noted
491 otherwise are from Sigma Aldrich.

492

493 **Cloning, protein expression and purification of GS-GN complex**

494 Genes encoding human GS1 (HsGS:NM 002103) and human GN1 (HsGN:NM 001184720)
495 mutant were cloned into pFL a vector[51]. A single 6 x His purification tag followed by a cleavable
496 site was engineered at the N-terminus of GN WT or GN Y195F mutant. For co-expression of
497 WT GS and mutants the genes encoding human GS1 and human GN1 (Y195F) were cloned
498 in pFastBac vectors, both with a 6x His purification tag followed by a TEV site at the N-
499 terminus. Recombinant bacmids were generated in DH10Bac™ cells. Virus amplification and
500 protein expression, in *Spodoptera frugiperda* (Sf9) cells and *Trichoplusia ni* (Tni) cells
501 respectively, were carried out using standard procedures[52]. For co-infection of pFastBac
502 clones, a 10:1 ratio of the GS:GN P2 virus ratio was used. A PCR-based site directed
503 mutagenesis was used to create the following mutants from the pFastBac GS1 construct:
504 W18A, R588A+R591A, Y600A, R603A, H610E, S614R. All of the alterations were confirmed
505 by DNA sequencing.

506

507 Cell pellets containing HsGS-GN, HsGS-GN(Y195F) and mutants were resuspended in lysis
508 buffer (50 mM Tris-HCl pH 7.6, 300 mM NaCl, 20 mM imidazole, 10% glycerol, 0.075% β-
509 mercaptoethanol, 1 mM benzamidine, 0.8 mM phenylmethyl sulfonyl fluoride (PMSF), 0.3
510 mg/mL lysozyme). Cells were lysed by sonication (1 second on, 3 seconds off for a total of 5
511 minutes) on ice and the lysate was cleared by centrifugation at 35,000*g* for 30 minutes at
512 4 °C. The clarified lysate was sonicated again (1 second on, 3 seconds off for a total of 1

513 minute), followed by filtering with a 0.45 µM filter (MerckMillipore). Filtered lysate was loaded
514 onto a pre-equilibrated 1 mL or 5 mL HisTrap HP column (GE Healthcare) charged with Ni^{2+}.
515 The loaded column was washed with four column volumes (CV) of low salt buffer (50 mM Tris-
516 HCl pH 7.6, 300 mM NaCl, 20 mM imidazole, 10% glycerol, 0.075% β-mercaptoethanol, 1mM
517 benzamidine), followed by four CV washes of high salt buffer (50 mM Tris-HCl pH 7.6, 500
518 mM NaCl, 20 mM imidazole, 10% glycerol, 0.075% β-mercaptoethanol, 1 mM benzamidine)
519 and finally 4 CV washes in low salt buffer. The column was then attached to the AKTA system
520 (GE Healthcare) and washed with low salt buffer. The protein was then eluted by applying an
521 imidazole gradient with elution buffer (50 mM Tris-HCl pH 7.6, 300 mM NaCl, 300 mM
522 imidazole, 10% glycerol, 0.075% β-mercaptoethanol, 1 mM benzamidine). The fractions
523 containing protein were analysed by SDS-PAGE and then pooled and dialysed overnight
524 (10,000 MWCO SnakeSkin dialysis tubing (Thermo Scientific)) at 4 °C in dialysis buffer with
525 TEV protease added (50 mM Tris-HCl pH 7.6, 150 mM NaCl, 20 mM imidazole, 10% glycerol,
526 0.075% β-mercaptoethanol, 1 mM benzamidine). The dialysed protein was re-loaded onto the
527 HisTrap column equilibrated with low salt buffer, for a Ni subtraction step. TEV cleaved protein
528 was eluted in the flow through and low salt washes. The flow through and first low salt wash
529 were pooled and concentrated using a VIVASPIN20 30,000 MWCO (Sartorius, Generon),
530 followed by centrifugation at 17,000*g* for 15 minutes at 4 °C. Protein was then injected onto a
531 16/600 or 10/300 Superdex200 column (GE Healthcare) equilibrated with gel filtration buffer
532 (25 mM HEPES pH 7.5, 150 mM NaCl, 1 mM TCEP, 10% glycerol). Fractions containing
533 protein were analysed by SDS-PAGE, and fractions containing GN were pooled, concentrated
534 and stored at -80 °C. Some fractions containing GS-GN complex were stored separately at -
535 80 °C and the remaining protein was pooled and concentrated before being stored at -80 °C.
536 Proteins were visualized by Coomassie blue staining, and glucosylated species were detected
537 using the periodic acid-Schiff (PAS) method (Glycoprotein staining kit, Thermo Scientific).
538

539 ***In vitro* dephosphorylation of GS-GN**

540 Protein phosphatase 1 (PP1) and lambda protein phosphatase (lambda PP) were bought from
541 MRC PPU Reagents and Services. Both have an N-terminal GST tag and lambda PP also
542 has a C-terminal 6x His tag. GS-GN complex was dephosphorylated in reactions containing
543 equal amounts of PP1 and lambda PP in 25 mM HEPES pH 7.5, 150 mM NaCl, 1 mM TCEP,
544 1 mM $MnCl_2$ and 10% glycerol for 30 minutes at 30 °C. For subsequent differential scanning
545 fluorimetry experiments, the phosphatases were removed by incubating the reactions with
546 GST beads for 1 hour at 4 °C. Reactions were then passed through an equilibrated 0.45 µm
547 Spin-X column (Costar, 0.45 µm cellulose acetate) and eluted by centrifugation at 16,000*g* for
548 2 minutes.

549

550 ***In vitro* deglycosylation**

551 GS-GN was incubated with α-amylase from human saliva (Sigma) to deglycosylate the
552 complex. Reactions contained 4 µM GS-GN with either 500 mU or 1 U α-amylase in buffer
553 containing 50 mM HEPES pH 7.5, 150 mM NaCl, 1 mM TCEP and 5 mM $CaCl_2$. Reactions
554 were incubated for 30 min, 1 hour or 2 hours at 37 °C and terminated by the addition of SDS-
555 PAGE loading dye.

556

557 **Negative stain electron microscopy – grid preparation and data collection**

558 HsGS-GN WT and Y195F were diluted in buffer (25 mM HEPES pH 7.5, 150 mM NaCl, 1 mM
559 TCEP, 10% glycerol) to concentrations between 0.01 and 0.02 mg/mL immediately before grid
560 preparation. Carbon-coated copper grids (Formvar/Carbon 300 mesh Cu, Agar Scientific)
561 were glow-discharged for 30 seconds, 10 mA and 0.39 mBar pressure (PELCO easiGlow, Ted
562 Pella). Grids were incubated for 1 minute with 6 µL sample, washed with H_2O three times and
563 stained twice with 2% w/v uranyl acetate for 20 seconds. Excess liquid was removed by
564 blotting with filter paper. Data was collected on a FEI Technai F20 electron microscope
565 operated at 120 keV, equipped with a FEI Ceta (CMOS CCD) camera.

566

567 **Negative stain electron microscopy – data processing**

568 RELION 3.0 was used for processing of negative stain-EM data[53]. Real-time contrast transfer
569 function (CTF) parameters were determined using gCTF[54]. Approximately 2,000 particles
570 were manually picked, extracted with a box size of 104 $Å^2$, then subjected to reference-free
571 2D classification to produce initial references to be used for auto-picking. The parameters for
572 auto-picking were optimized and 92,580 particles were extracted. The extracted particles were
573 used for iterative rounds of reference-free 2D classification. Based on visual inspection, best
574 quality 2D average classes were selected to generate a *de novo* 3D initial model, which was
575 used as a reference in unsupervised 3D classification. These classes were then subjected to
576 3D refinement to generate a final EM density map.

577

578 **Cryo-electron microscopy – grid preparation and data collection**

579 Quantifoil R2/2 Cu300 or Quantifoil R1.2/1.3 Cu300 (Quantifoil Micro Tools) grids were glow-
580 discharged using the GloQube plasma cleaner (Quorum) at 40 mA for 30 seconds, for GS-
581 GN(Y195F) and GS-GN respectively. A FEI Vitrobot IV was equilibrated at 4 °C at 100%
582 relative humidity. GS-GN(Y195F) complex was diluted in buffer (25 mM HEPES pH7.5, 150
583 mM NaCl, 1 mM TCEP) to 0.8 mg/mL (6.59 µM) containing 1.5% glycerol immediately before
584 3 µL was added to the grid. GS-GN was diluted to 0.36 mg/mL (2.97 µM) containing 8%

585 glycerol. This was followed by immediate blotting and plunge-freezing into liquid ethane cooled
586 by liquid nitrogen.
587
588 All data was collected on a FEI Titan KRIOS transmission electron microscope at 300 keV.
589 For GS-GN(Y195F), A FEI Falcon IV direct electron detector with an energy filter (10 eV) was
590 used in counting mode[55]. A dose per physical pixel/s used resulting in a total dose of 34.8
591 e/Å^2, fractionated across 128 EPU frames. This was then grouped into 21 frames, resulting in
592 a dose per frame of 0.8 e/Å^2. Magnification was 165,000x resulting in a pixel size of 0.71
593 Å/pixel. Eight exposures per hole was taken and the defocus values ranged from -1 µm to -
594 2.2 µm. 20,841 movies were recorded using the EPU automated acquisition software (v2.13).
595
596 For GS-GN, a FEI Falcon III direct electron detector was used in integrating mode[55]. The total
597 electron dose was 85 e/Å^2, a magnification of 75,000x was used and a final calibrated object
598 sampling of 1.065 Å/pixel. Each movie had a total exposure time of 1.6 seconds, collected
599 over 47 fractions with an electron dose of 1.8 e/Å^2 per fraction. One exposure per hole was
600 taken and the defocus values ranged from -1.7 µm to -3.1 µm. 3,009 movies were recorded
601 using the EPU automated acquisition
602
603 **Cryo-electron microscopy – data processing**
604
605 For GS-GN(Y195F), drift-corrected averages of each movie were created using MotionCor2[56]
606 and real-time contrast transfer function (CTF) parameters were determined using CTFFIND-
607 4.1[57]. Both motion correction and CTF estimation were carried out on-the fly[55]. 1,883,188
608 particles were picked using the PhosaurusNet general model in crYOLO[58] v1.6.1. Particles
609 were imported into RELION 3.1 and extracted and binned by 2. These particles were subjected
610 to 2D classification. 1,188,332 particles selected after 2D classification were subjected to 3D
611 classification, applying D2 symmetry. Carrying all "good"/unambiguous classes forward,
612 739,232 particles were un-binned to a box size of 288 pixels and subjected to 3Drefinement
613 and postprocessing, generating a map at 2.92 Å. Followed by iterative rounds of per particle
614 contrast transfer function refinement and Bayesian particle polishing to generate a map at
615 2.62 Å (**Supplementary Fig. 5**). Final resolutions were determined using the gold-standard
616 Fourier shell correlation criterion (FSC=0.143). Local resolution was estimated using the local
617 resolution feature in RELION.
618
619 To prevent interpretation of any artefacts created by applying D2 symmetry, the data was also
620 processed in C1 symmetry (**Supplementary Fig. 6)**. The same particles after 2D classification
621 were subjected to 3D classification without applying symmetry. High quality classes containing

783,177 particles were un-binned to a box size of 288 pixels and then subjected to 3D refinement and postprocessing, to generate a 3.1 Å map. Following iterative rounds of contrast transfer function refinement and Bayesian particle polishing to generate a 2.8 Å map.

To elucidate the movement of phosphoregulatory regions, an alignment free 3D classification with a mask containing the "spike" density was performed, using a regularisation parameter T of 60[59] (**Supplementary Fig. 5f and 5g**).

To explore the heterogeneity in the dataset, the 3D variability analysis[44] tool in cryoSPARC v3.2.0[45] was used. The 739,232 particles after 3D classification were imported into cryoSPARC and homogenous refinement with a mask with no symmetry application was performed. The subsequent particles were used in the 3D variability analysis to solve 3 modes, using C1 symmetry and with a filter resolution of 5 Å. The subsequent frames were visualized in Chimera[60]. 1 mode is shown in **Movie S1**.

For GS-GN, drift-corrected averages of each movie were created using MotionCor2[56] and real-time contrast transfer function (CTF) parameters were determined using gCTF[54]. 250,250 particles were picked using the PhosaurusNet general model in crYOLO[58] v1.3.5. Particles were then imported into RELION 3.0[53], extracted with a box size of 220 pixels and subjected to reference-free 2D classification. 84,557 particles selected after 2D classification were subjected to 3D classification. 36,972 particles (from 2 classes) were subjected to 3D refinement and postprocessing, generating a map at 6.0 Å (**Supplementary Fig. 6e and 6e**).

Model building and refinement

A preliminary model of human GS was generated by AlphaFold[43] (accessed 1 October 2021) and a preliminary model of last 34 residues of human GN was created by Phyre2[61]. These preliminary models were rigid body fitted into the cryo-EM density in UCSF Chimera[60]. The model was then built using iterative rounds of manual building in COOT[62] and real space refinement in PHENIX v1.19[63].

Visualisation, structure analysis and sequence alignments

Visualisation and structure analysis were performed using ChimeraX[64] or Chimera[60]. Multiple sequence alignments were performed using MUSCLE[65] and displayed and edited using ALINE v1.0.025[66].

657 **Mass photometry**

658 Mass photometry experiments were performed using a Refyn One^{MP} mass photometer.
659 Immediately prior to mass photometry measurements, proteins were diluted in 25 mM HEPES
660 pH 7.5, 150 mM NaCl, 1 mM TCEP for a final concentration of 50 nM. For each measurement,
661 (16 µL) buffer was added to a well and the focus point was found and adjusted when
662 necessary. Protein (4 µL) was then added to the buffer droplet, the sample was mixed and
663 movies of 60 seconds were recorded using AcquireMP. Data were analysed using
664 DiscoverMP.

665

666 **Differential Scanning Fluorimetry**

667 Thermal shift assays were performed using an Applied Biosystems QuantStudio 3 Real-Time
668 PCR system. SYPRO™ Orange (Invitrogen) was used as a fluorescence probe. Proteins were
669 diluted in 25 mM HEPES pH 7.5, 150 mM NaCl, 1 mM TCEP to a final concentration of 1 µM.
670 Varied concentrations of G6P were added and the reaction was incubated at room
671 temperature for 30 minutes. SYPRO Orange was diluted in 25 mM HEPES pH 7.5, 150 mM
672 NaCl, 1 mM TCEP to a final concentration of 2.5 X, in a total reaction volume of 20 µL. The
673 temperature was raised in 0.018 °C intervals from 20 °C to 95 °C. Data were analysed using
674 Protein Thermal Shift™ v1.4.

675

676 **Tandem mass spectrometry**

677 Concentrated purified protein complexes (6.75 µg) were diluted 30-fold in 25 mM ammonium
678 bicarbonate pH 8.0 before being subject to reduction with dithiothreitol and alkylation with
679 iodoacetamide, as previously described[67]. The eluent was equally divided into three for
680 digestion with either: 33:1 (w/w) trypsin gold (Promega), 25:1 (w/w) chymotrypsin (Promega),
681 or 10:1 (w/w) elastase (Promega), using the manufacturer's recommended temperatures for
682 18 hours with 600 rpm shaking. Digests were then subject to in-house packed, strong cation
683 exchange stage tip clean-up, as previously described by[68]. Dried peptides were solubilized in
684 20 µl of 3% (v/v) acetonitrile and 0.1% (v/v) TFA in water, sonicated for 10 minutes, and
685 centrifuged at 13,000*g* for 15 minutes at 4 °C being separated using an Ultimate 3000 nano
686 system (Dionex) by reversed-phase HPLC, over a 60-minute gradient, as described in[67]. All
687 data acquisition was performed using a Thermo Orbitrap Fusion Lumos Tribrid mass
688 spectrometer (Thermo Scientific), with higher-energy C-trap dissociation (HCD) fragmentation
689 set at 32% normalized collision energy for 2+ to 5+ charge states. MS1 spectra were acquired
690 in the Orbitrap (60K resolution at 200 *m/z*) over a range of 350 to 1400 *m/z*, AGC target =
691 standard, maximum injection time = auto, with an intensity threshold for fragmentation of $2e^4$.
692 MS2 spectra were acquired in the Orbitrap (30K resolution at 200 *m/z*), AGC target = standard,

693 maximum injection time = dynamic. A dynamic exclusion window of 20 seconds was applied
694 at a 10 ppm mass tolerance. Data was analysed by Proteome Discoverer 1.4 using the UniProt
695 Human reviewed database (updated April 2020) with fixed modification =
696 carbamidomethylation (C), variable modifications = oxidation (M) and phospho (S/T/Y),
697 instrument type = electrospray ionization–Fourier-transform ion cyclotron resonance (ESI-
698 FTICR), MS1 mass tolerance = 10 ppm, MS2 mass tolerance = 0.01 Da, and the *ptm*RS node
699 on; set to a score > 99.0.
700

701 **Protein Identification Mass Spectrometry**

702 10 µg of purified protein was separated by SDS-PAGE (10% resolving, 4% stacking) before
703 colloidal Coomassie staining overnight and thorough washing in milliQ water[69]. A scalpel was
704 used to excise the major band at ~85 kDa, and incremental bands spanning 43-55, 55-72, 95-
705 130 and 130+ kDa. Bands were washed in 500 µL HPLC H_2O for 10 minutes shaking at 1500
706 rpm, room temperature. Bands were then washed in 500 µL of 100 mM ammonium
707 bicarbonate with water bath sonication, as before, for 10 minutes, before an equal volume of
708 HPLC acetonitrile was added and sonication repeated. Previous two wash steps were
709 repeated until the gel pieces were clear. 100 µL of reduction solution (4 mM dithiothreitol in
710 50 mM ammonium bicarbonate) was added to each gel slice and heated to 60 ^{o}C for 10
711 minutes with 600 rpm shaking. A final concentration of 16.4 mM iodoacetamide was added
712 and incubated in darkness at room temperature for 30 minutes, before quenching by addition
713 of 100 mM dithiothreitol to make a final concentration of 7 mM. All liquid was removed before
714 dehydrating the gel slice by addition of 100 µL HPLC acetonitrile and shaking 1500 rpm at
715 room temperature for 15 minutes. Dehydrydration was repeated until gel slices were opaque
716 white and left open lid to dry completely (~15 minutes). 0.5 µg of trypsin in 40 mM ammonium
717 bicarbonate was added to the dehydrated gel slices and incubated room temperature for 15
718 minutes. Residual liquid was removed and 100 µL of incubation solution (40 mM ammonium
719 bicarbonate, 5% acetonitrile) added and incubated overnight at 37 ^{o}C with 600 rpm shaking.
720 An equal volume of acetonitrile was added and left to shake for an additional 30 minutes. Gel
721 slices were briefly centrifuged and supernatant collected. Supernatant was dried to
722 completion, resuspended and analysed by LC-MS/MS as described before.
723

724 **Glycogen synthase activity assay**

725 1 µg of purified protein was diluted in ice cold lysis buffer (270 mM sucrose, 50 mM Tris-HCl
726 (pH 7.5), 1 mM EDTA, 1 mM EGTA, 1% (v/v) Triton X-100, 20 mM glycerol-2-phosphate, 50
727 mM NaF, 5 mM $Na_4P_2O_7$, 1 mM DTT, 0.1 mM PMSF, 1 mM benzamidine, 1 mg/mL
728 microcystin-LR, 2 mg/mL leupeptin, and 2 mg/mL pepstatin A) to a total volume of 100 µL. 20

729 μL of the protein was added to 80 μL of the assay buffer (25 mM Tris-HCl (pH 7.8), 50 mM
730 NaF, 5 mM EDTA, 10 mg/ml glycogen, 1.5 mM UDP-glucose, 0.125% (v/v) β-mercaptoethanol
731 and 0.15 mCi/mmol D-[^{14}C]-UDP-glucose (American Radiolabelled Chemicals, Inc., ARC
732 0154) with 0 and 12.5 mM G6P. Reactions were incubated for 20 minutes at 30 °C with mild
733 agitation at 300 rpm. The reactions were stopped by spotting 90 μL of the reaction mix onto
734 2.5 cm x 2.5 cm squares of filter paper (Whatman 3MM) which were immediately immersed in
735 ice cold 66% ethanol and left to incubate with mild agitation for 20 minutes. The filter papers
736 were washed thrice more in 66% ethanol for 20 minutes each and rinsed in acetone. The dried
737 filters were subjected to scintillation counting.
738
739 **Statistical Analysis**
740 Data are reported as mean ± standard error of the mean (SEM) and statistical analysis was
741 performed using GraphPad Prism software. As indicated in the respective figure legends, one-
742 way or two-way analysis of variance was performed with Tukey's post hoc test. Statistical
743 significance was set at $p<0.05$.
744
745 **Immunoblotting**
746 Purified proteins were denatured in Laemmli buffer at 100 °C for 5 minutes. 100 ng of the
747 protein was separated by SDS-PAGE on 4-10% gel and transferred onto nitrocellulose
748 membranes (#926-31090, LiCOR). Membranes were blocked for 45 minutes at room
749 temperature in 5% skim milk (Sigma, 1153630500) followed by incubation in TBST (10 mM
750 Tris (pH 7.6), 137 mM NaCl, and 0.1% (v/v) Tween-20) containing 5% (w/v) BSA and the
751 primary antibody overnight at 4 ºC. The membranes were incubated for 45 minutes in HRP
752 conjugated secondary antibodies diluted 1:10,000 in 3% skim milk, after extensive washing in
753 TBST. The membranes were imaged using enhanced chemiluminescence (ECL) reagent (GE
754 Healthcare). For total protein staining of blots, Revert™700 Total Protein Stain (LiCOR) was
755 used.
756
757 For the validation of pGS S8 antibody (YenZyme, 1st cycle, YZ7516) HEK293FT cells were
758 co-transfected with 900 ng of GS (WT) or GS S8A along with GST tagged-GN. After 40 hours,
759 transfected cells were harvested for protein. The blots were probed with pGS S8 antibody
760 incubated with 20 μg of GS peptide (**Supplementary Fig. 4c**).
761
762
763
764

Data availability:

The cryo-EM maps have been deposited in the Electron Microscopy Data Bank under the accession code EMDB-14587. Coordinates have been deposited in the Protein Data Bank under the accession code 7ZBN.

Author contributions:

L.M. performed molecular biology, protein production, electron microscopy, differential scanning fluorimetry and mass photometry experiments, D.B. performed glycogen synthase activity and western blot assays, L.A.D. performed phosphorylation mapping and mass spectrometry experiments and C.B., S.V. and D.P.M. provided support with structural biology and protein production. L.M. and E.Z. drafted the manuscript with input from D.B., K.S., L.A.D. and C.E.E. and all authors revised it. J.P., C.E.E., C.H., J.B., N.A.R., H.K., K.S. and E.Z. provided supervision and project management. E.Z., K.S., C.E.E., C.H. and J.B. designed and interpreted data in consultation with all authors.

Acknowledgments:

L.M. is supported by an MRC Discovery Medicine North (DiMeN) iCASE studentship co-funded by UKRI and Vertex Pharmaceuticals. D.B. is supported by an International Postdoctoral Fellowship funded by the Novo Nordisk Foundation (NNF) Center for Basic Metabolic Research. C.E.E. and L.A.D. were supported by grants from BBSRC (BB/S018514/1, BB/M012557/1, BB/R000182/1). E.Z. was supported by a Sir Henry Dale Fellowship from the Wellcome Trust & Royal Society (200523/Z/16/Z) and Royal Society grant RG170407. The Astbury cryo-EM Facility is funded by a University of Leeds ABSL award and Wellcome Trust grants (108466/Z/15/Z and 221524/Z/20/Z). The NNF Center for Basic Metabolic Research is an independent Research Center at the University of Copenhagen, Denmark, and partially funded by an unconditional donation from NNF (Grant number NNF18CC0034900).

Conflict of Interest

The authors report no conflicts of interest.

798 **References**

799

800 1. Roach, P. J., Depaoli-Roach, A. A., Hurley, T. D. & Tagliabracci, V. S. Glycogen and
801 its metabolism: some new developments and old themes. *Biochem. J.* **441,** 763–787
802 (2012).
803 2. Roach, P. J. Glycogen and its metabolism. *Curr. Mol. Med.* **2,** 101–120 (2002).
804 3. Pitcher, J., Smythe, C., Campbell, D. G. & Cohen, P. Identification of the 38-kDa
805 subunit of rabbit skeletal muscle glycogen synthase as glycogenin. *European Journal*
806 *of Biochemistry* **169,** 497–502 (1987).
807 4. Zeqiraj, E. & Sicheri, F. Getting a handle on glycogen synthase – Its interaction with
808 glycogenin. *Molecular Aspects of Medicine* **46,** 63–69 (2015).
809 5. Skurat, A. V., Dietrich, A. D. & Roach, P. J. Interaction between glycogenin and
810 glycogen synthase. *Archives of Biochemistry and Biophysics* **456,** 93–97 (2006).
811 6. Pitcher, J., of, C. S. E. J.1988. Glycogenin is the priming glucosyltransferase required
812 for the initiation of glycogen biogenesis in rabbit skeletal muscle. *European Journal of*
813 *Biochemistry* **176,** 391–395 (1988).
814 7. Ryu, J.-H. *et al.* Comparative structural analyses of purified glycogen particles from
815 rat liver, human skeletal muscle and commercial preparations. *International Journal of*
816 *Biological Macromolecules* **45,** 478–482 (2009).
817 8. Ashcroft, F. M., Rohm, M., Clark, A. & Brereton, M. F. Is Type 2 Diabetes a Glycogen
818 Storage Disease of Pancreatic β Cells? *Cell Metabolism* **26,** 17–23 (2017).
819 9. Kohler, L., Puertollano, R. & Raben, N. Pompe Disease: From Basic Science to
820 Therapy. *Neurotherapeutics* **15,** 928–942 (2018).
821 10. García-Gimeno, M., Knecht, E. & Sanz, P. Lafora Disease: A Ubiquitination-Related
822 Pathology. *Cells* **7,** 87–17 (2018).
823 11. Malfatti, E. *et al.* A new muscle glycogen storage disease associated with glycogenin-
824 1 deficiency. *Ann Neurol.* **76,** 891–898 (2014).
825 12. Pursell, N. *et al.* Inhibition of Glycogen Synthase II with RNAi Prevents Liver Injury in
826 Mouse Models of Glycogen Storage Diseases. *Mol Ther* **26,** 1771–1782 (2018).
827 13. Ashe, K. M. *et al.* Inhibition of glycogen biosynthesis via mTORC1 suppression as an
828 adjunct therapy for Pompe disease. *Molecular Genetics and Metabolism* **100,** 309–
829 315 (2010).
830 14. Turnbull, J. *et al.* PTG depletion removes Lafora bodies and rescues the fatal epilepsy
831 of Lafora disease. *PLoS Genet* **7,** e1002037 (2011).
832 15. Pederson, B. A. *et al.* Inhibiting glycogen synthesis prevents Lafora disease in a
833 mouse model. *Ann Neurol.* **74,** 297–300 (2013).

834 16. Varea, O., Duran, J., Aguilera, M., Prats, N. & Guinovart, J. J. Suppression of
835 glycogen synthesis as a treatment for Lafora disease: Establishing the window of
836 opportunity. *Neurobiol Dis* **147,** 105173 (2021).
837 17. Mu, J., Skurat, A. V. & Roach, P. J. Glycogenin-2, a Novel Self-glucosylating Protein
838 Involved in Liver Glycogen Biosynthesis. *J. Biol. Chem.* **272,** 27589–27597 (1997).
839 18. Curtino, J. A. & Aon, M. A. From the seminal discovery of proteoglycogen and
840 glycogenin to emerging knowledge and research on glycogen biology. *Biochem. J.*
841 **476,** 3109–3124 (2019).
842 19. Lairson, L. L., Henrissat, B., Davies, G. J. & Withers, S. G. Glycosyltransferases:
843 Structures, Functions, and Mechanisms. *Annu. Rev. Biochem.* **77,** 521–555 (2008).
844 20. Gibbons, B. J., Roach, P. J. & Hurley, T. D. Crystal Structure of the Autocatalytic
845 Initiator of Glycogen Biosynthesis, Glycogenin. *Journal of Molecular Biology* **319,**
846 463–477 (2002).
847 21. Chaikuad, A. *et al.* Conformational plasticity of glycogenin and its maltosaccharide
848 substrate during glycogen biogenesis. *Proceedings of the National Academy of*
849 *Sciences* **108,** 21028–21033 (2011).
850 22. Zeqiraj, E. *et al.* Structural basis for the recruitment of glycogen synthase by
851 glycogenin. *Proceedings of the National Academy of Sciences* **111,** E2831–E2840
852 (2014).
853 23. Skurat, A. V., Wang, Y. & Roach, P. J. Rabbit skeletal muscle glycogen synthase
854 expressed in COS cells. Identification of regulatory phosphorylation sites. *J. Biol.*
855 *Chem.* **269,** 25534–25542 (1994).
856 24. Wilamowitz-Moellendorff, von, A. *et al.* Glucose-6-phosphate-mediated activation of
857 liver glycogen synthase plays a key role in hepatic glycogen synthesis. *Diabetes* **62,**
858 4070–4082 (2013).
859 25. Browner, M. F., Nakano, K., Bang, A. G. & Fletterick, R. J. Human muscle glycogen
860 synthase cDNA sequence: a negatively charged protein with an asymmetric charge
861 distribution. *Proceedings of the National Academy of Sciences* **86,** 1443–1447 (1989).
862 26. Nuttall, F. Q., Gannon, M. C., Bai, G. & Lee, E. Y. Primary structure of human liver
863 glycogen synthase deduced by cDNA cloning. *Archives of Biochemistry and*
864 *Biophysics* **311,** 443–449 (1994).
865 27. Buschiazzo, A. *et al.* Crystal structure of glycogen synthase: homologous enzymes
866 catalyze glycogen synthesis and degradation. *The EMBO Journal* **23,** 3196–3205
867 (2004).
868 28. Skurat, A. V., Peng, H. L., Chang, H. Y., Cannon, J. F. & Roach, P. J. Rate-
869 determining steps in the biosynthesis of glycogen in COS cells. *Archives of*
870 *Biochemistry and Biophysics* **328,** 283–288 (1996).

871 29. Hunter, R. W., Treebak, J. T., Wojtaszewski, J. F. P. & Sakamoto, K. Molecular
872 Mechanism by Which AMP-Activated Protein Kinase Activation Promotes Glycogen
873 Accumulation in Muscle. *Diabetes* **60,** 766–774 (2011).
874 30. Baskaran, S., Roach, P. J., Depaoli-Roach, A. A. & Hurley, T. D. Structural basis for
875 glucose-6-phosphate activation of glycogen synthase. *Proc. Natl. Acad. Sci. U.S.A.*
876 **107,** 17563–17568 (2010).
877 31. Picton, C., Woodgett, J., Hemmings, B. & Cohen, P. Multisite phosphorylation of
878 glycogen synthase from rabbit skeletal muscle. Phosphorylation of site 5 by glycogen
879 synthase kinase-5 (casein kinase-II) is a prerequisite for phosphorylation of sites 3 by
880 glycogen synthase kinase-3. *FEBS Lett* **150,** 191–196 (1982).
881 32. Roach, P. J. Multisite and hierarchal protein phosphorylation. *J. Biol. Chem.* **266,**
882 14139–14142 (1991).
883 33. Roach, P. J. Control of glycogen synthase by hierarchal protein phosphorylation.
884 *FASEB J* **4,** 2961–2968 (1990).
885 34. Mahalingan, K. K., Baskaran, S., Depaoli-Roach, A. A., Roach, P. J. & Hurley, T. D.
886 Redox Switch for the Inhibited State of Yeast Glycogen Synthase Mimics Regulation
887 by Phosphorylation. *Biochemistry* **56,** 179–188 (2017).
888 35. Hunter, R. W., Zeqiraj, E., Morrice, N., Sicheri, F. & Sakamoto, K. Expression and
889 purification of functional human glycogen synthase-1:glycogenin-1 complex in insect
890 cells. *PROTEIN EXPRESSION AND PURIFICATION* **108,** 23–29 (2015).
891 36. Khanna, M. *et al.* Expression and purification of functional human glycogen synthase-
892 1 (hGYS1) in insect cells. *PROTEIN EXPRESSION AND PURIFICATION* **90,** 78–83
893 (2013).
894 37. Smythe, C., Caudwell, F. B., Ferguson, M. & Cohen, P. Isolation and structural
895 analysis of a peptide containing the novel tyrosyl-glucose linkage in glycogenin. *The*
896 *EMBO Journal* **7,** 2681–2686 (1988).
897 38. Rodriguez, I. R. & Whelan, W. J. A novel glycosyl-amino acid linkage: rabbit-muscle
898 glycogen is covalently linked to a protein via tyrosine. *Biochemical and Biophysical*
899 *Research Communications* **132,** 829–836 (1985).
900 39. Bouskila, M. *et al.* Allosteric Regulation of Glycogen Synthase Controls Glycogen
901 Synthesis in Muscle. *Cell Metabolism* **12,** 456–466 (2010).
902 40. McManus, E. J. *et al.* Role that phosphorylation of GSK3 plays in insulin and Wnt
903 signalling defined by knockin analysis. *The EMBO Journal* **24,** 1571–1583 (2005).
904 41. Hornbeck, P. V. *et al.* PhosphoSitePlus, 2014: mutations, PTMs and recalibrations.
905 *Nucleic Acids Res* **43,** D512–20 (2015).

906 42. Wang, Y. & Roach, P. J. Inactivation of rabbit muscle glycogen synthase by glycogen
907 synthase kinase-3. Dominant role of the phosphorylation of Ser-640 (site-3a). *J. Biol.*
908 *Chem.* **268,** 23876–23880 (1993).
909 43. Jumper, J. *et al.* Highly accurate protein structure prediction with AlphaFold. *Nature*
910 **596,** 583–589 (2021).
911 44. Punjani, A. & Fleet, D. J. 3D variability analysis: Resolving continuous flexibility and
912 discrete heterogeneity from single particle cryo-EM. *Journal of Structural Biology* **213,**
913 107702 (2021).
914 45. Punjani, A., Rubinstein, J. L., Fleet, D. J. & Brubaker, M. A. cryoSPARC: algorithms
915 for rapid unsupervised cryo-EM structure determination. *Nat Methods* **14,** 290–296
916 (2017).
917 46. Ramlaul, K., Palmer, C. M. & Aylett, C. H. S. A Local Agreement Filtering Algorithm
918 for Transmission EM Reconstructions. *Journal of Structural Biology* **205,** 30–40
919 (2019).
920 47. Hanashiro, I. & Roach, P. J. Mutations of muscle glycogen synthase that disable
921 activation by glucose 6-phosphate. *Archives of Biochemistry and Biophysics* **397,**
922 286–292 (2002).
923 48. Palm, D. C., Rohwer, J. M. & Hofmeyr, J.-H. S. Regulation of glycogen synthase from
924 mammalian skeletal muscle - a unifying view of allosteric and covalent regulation.
925 *FEBS J* **280,** 2–27 (2012).
926 49. Baskaran, S. *et al.* Multiple glycogen-binding sites in eukaryotic glycogen synthase
927 are required for high catalytic efficiency toward glycogen. *J. Biol. Chem.* **286,** 33999–
928 34006 (2011).
929 50. Chikwana, V. M. *et al.* Structural basis for 2'-phosphate incorporation into glycogen by
930 glycogen synthase. *Proc. Natl. Acad. Sci. U.S.A.* **110,** 20976–20981 (2013).
931 51. Fitzgerald, D. J. *et al.* Protein complex expression by using multigene baculoviral
932 vectors. *Nat Methods* **3,** 1021–1032 (2006).
933 52. Zeqiraj, E. *et al.* Higher-Order Assembly of BRCC36-KIAA0157 Is Required for DUB
934 Activity and Biological Function. *Mol Cell* **59,** 970–983 (2015).
935 53. Zivanov, J. *et al.* New tools for automated high-resolution cryo-EM structure
936 determination in RELION-3. *eLIFE* **7,** (2018).
937 54. Zhang, K. Gctf: Real-time CTF determination and correction. *Journal of Structural*
938 *Biology* **193,** 1–12 (2016).
939 55. Thompson, R. F., Iadanza, M. G., Hesketh, E. L., Rawson, S. & Ranson, N. A.
940 Collection, pre-processing and on-the-fly analysis of data for high-resolution, single-
941 particle cryo-electron microscopy. *Nat Protoc* **14,** 100–118 (2018).

942 56. Zheng, S. Q. *et al.* MotionCor2: anisotropic correction of beam-induced motion for
943 improved cryo-electron microscopy. *Nat Methods* **14,** 331–332 (2017).
944 57. Rohou, A. & Grigorieff, N. CTFFIND4: Fast and accurate defocus estimation from
945 electron micrographs. *Journal of Structural Biology* **192,** 216–221 (2015).
946 58. Wagner, T. *et al.* SPHIRE-crYOLO is a fast and accurate fully automated particle
947 picker for cryo-EM. *Commun Biol* **2,** 218–13 (2019).
948 59. Scheres, S. H. W. in *Cryo-EM, Part B: 3-D Reconstruction* **482,** 295–320 (Elsevier,
949 2010).
950 60. Pettersen, E. F. *et al.* UCSF Chimera--a visualization system for exploratory research
951 and analysis. *J Comput Chem* **25,** 1605–1612 (2004).
952 61. Kelley, L. A., Mezulis, S., Yates, C. M., Wass, M. N. & Sternberg, M. J. E. The Phyre2
953 web portal for protein modeling, prediction and analysis. *Nat Protoc* **10,** 845–858
954 (2015).
955 62. Emsley, P., Lohkamp, B., Scott, W. G. & Cowtan, K. Features and development of
956 Coot. *Acta Crystallogr D Biol Crystallogr* **66,** 486–501 (2010).
957 63. Adams, P. D. *et al.* PHENIX: a comprehensive Python-based system for
958 macromolecular structure solution. *Acta Crystallogr D Biol Crystallogr* **66,** 213–221
959 (2010).
960 64. Pettersen, E. F. *et al.* UCSF ChimeraX: Structure visualization for researchers,
961 educators, and developers. *Protein Sci* **30,** 70–82 (2021).
962 65. Madeira, F. *et al.* The EMBL-EBI search and sequence analysis tools APIs in 2019.
963 *Nucleic Acids Res* **47,** W636–W641 (2019).
964 66. Bond, C. S. & Schüttelkopf, A. W. ALINE: a WYSIWYG protein-sequence alignment
965 editor for publication-quality alignments. *Acta Crystallogr D Biol Crystallogr* **65,** 510–
966 512 (2009).
967 67. Ferries, S. *et al.* Evaluation of Parameters for Confident Phosphorylation Site
968 Localization Using an Orbitrap Fusion Tribrid Mass Spectrometer. *J Proteome Res*
969 **16,** 3448–3459 (2017).
970 68. Daly, L. A. *et al.* Oxygen-dependent changes in binding partners and post-
971 translational modifications regulate the abundance and activity of HIF-1α/2α. *Sci*
972 *Signal* **14,** (2021).
973 69. Candiano, G. *et al.* Blue silver: a very sensitive colloidal Coomassie G-250 staining for
974 proteome analysis. *Electrophoresis* **25,** 1327–1333 (2004).